Paper

Integrating PWM amplifier with the design of mechatronic systems for energy-efficient precision motion

Shingo Ito[*]   Non-member,   Stefan Pirker[**]   Non-member
Georg Schitter[*]   Non-member

This paper proposes an integrated mechatronic system design to realize insensitivity to the current ripple of a switching current amplifier that drives electromagnetic actuators in high-precision motion systems. Switching current amplifiers are desirable for high energy efficiency with a concern that the resulting current ripple impairs the achievable positioning resolution. To eliminate this concern, a motion system is developed based on a flexure-guided voice coil actuator, which is driven by a switching current amplifier. A resonator is mounted onto the mover, creating an antiresonance at 11.3 kHz. This antiresonance is used to absorb the mover vibrations stemming from the current ripple. For this purpose, pulse width modulation (PWM) is used in the current amplifier such that the switching frequency is accurately tuned to the antiresonant frequency. Experiments reveal that the developed switching current amplifier reduces the power loss by a factor of 5.6 in comparison with a linear current amplifier. However, the switching current amplifier creates a current ripple of 0.77 A and oscillates the mover, resulting in a parasitic vibration of 5.1 nm. The use of the antiresonance successfully eliminates this vibration, decreasing the positioning error by a factor of three to 1.6 nm.

Keywords: Nanopositioner, Motion control, PWM amplifier, Mechatronics.

1. Introduction

Motion systems with nanometer resolution are indispensable for many applications, such as instrumentation [1], vibration isolation [2], and additive manufacturing [3]. For the desired motion, high-precision actuators are integrated in these systems [4]. Particularly, electromagnetic actuators, such as Lorentz actuators (e.g. voice coil actuators) [5] or hybrid reluctance actuators [6], are often utilized for a relatively large motion of more than tens of micrometers. These actuators can be guided by flexures for compactness. For the reduction of the systems' running cost, as well as for the sustainability of the society [7], it is desired to improve the energy efficiency of the motion systems, and the energy dissipation of major components needs to be decreased without impairing the motion precision.

One of the major components that dissipate energy is the power amplifiers (PAs) used in current amplifiers to drive the actuators. For high quality motion, PAs need to output the coil current with low noise, and linear PAs are typically selected for their smooth output current without distortion and high-frequency harmonics [8]. However, linear PAs dissipate a lot of energy because of the voltage over the internal transistors to output the coil current, restricting the energy efficiency. For example, the energy efficiency of Class-A PAs are theoretically up to 50 % only [9]. This poor energy efficiency is problematic also for the system's compactness because large heat sinks for cooling and sufficient power supplies are necessary [9].

The energy efficiency can be improved by using switching PAs [9], which set the drain-to-source voltage of the transistors ideally to zero while they provide any drain current. This operation theoretically dissipates no energy at a steady state. Consequently, switching PAs achieve high energy efficiency of 70-90 % dependent on the application [10]. However, the internal transistors need to be switched on and off at a frequency of more than a few kilohertz to generate arbitrary coil current. This switching is problematic, resulting in the coil current ripple, which leads to force ripple that impairs the positioning resolution of the high-precision motion system. Countermeasures against this problem include low-pass and notch filters (e.g. LCL filters) [11] and multilevel switching PAs [12], which increase the number of components. While the current ripple can be deceased by increasing the switching frequency, major concerns are electromagnetic interference (EMI) influencing the surrounding precision devices [13], and the energy loss due to the increased number of switching (i.e, switching loss).

In summary, previously proposed methods mainly use the design freedom of electronics and control although motion systems are a mechatronic system. While mechatronic systems use technologies in interdisciplinary fields for high performance, actuators and PAs are typically simply combined in a motion system, rather than integrated by considering the interaction of all the components for performance synergy.

[*] Christian Doppler Laboratory for Precision Engineering for Automated In-Line Metrology, Automation and Control Institute (ACIN), TU Wien,
Gusshausstrasse 27-29, A-1040 Vienna, Austria
[**] Automation and Control Institute (ACIN), TU Wien,
Gusshausstrasse 27-29, A-1040 Vienna, Austria

1

This paper proposes an integrated mechatronic system design with a switching PA. It utilizes freedom in the mechanical and electronic design for motion systems with high energy efficiency and high positioning resolution. In the proposed design, high energy efficiency and high positioning resolution are realized by developing a system with insensitivity to the force ripple induced by the switching PA. This is implemented by integrating a resonator to create a mechanical notch filter. In the electronic design, pulse width modulation (PWM) is utilized to drive the PA at a constant switching frequency, which is tuned to the notch frequency for the force ripple insensitivity. In other words, the mechanical system is tailored for the PWM-driven actuator and vice versa in the motion system by considering the interaction of its components in advance for high performance.

Section 2 introduces an experimental setup to demonstrate the proposed mechatronic system design. Section 3 discusses the mechanical design and analysis to implement the mechanical filter. Section 4 presents the switching current amplifier, and its performance is evaluated in comparison with a benchmarking linear current amplifier. Position feedback control is designed in Sec. 5 to reject disturbances for high-precision positioning. Sec. 6 presents experimental results, followed by the conclusion in Sec. 7.

2. System description

Fig. 1 shows the setup for the experimental demonstration of the proposed mechatronic system design. For high precision vertical (Z-axis) motion, a Lorentz actuator with a motor constant of $K_m = 7.2$ N/A (AVA 2-20, Akribis Systems, Singapore) is selected. Its coil has an inductance and resistance of 1.6 mH and 3.4 Ω, respectively, and its maximum coil current is 1.4 A$_{rms}$. While the coil is fixed to the mechanical ground, its magnet assembly is guided by two leaf-spring flexures as the mover. The aim of the paper is to control the mover position z_m with high resolution by using the actuator in an energy efficient way. For this purpose, a switching amplifier is developed as discussed in Section 4. To filter the force ripple induced by its switching, a resonator is mounted on the mover to realize a mechanical filter. The design of the resonator as well as the flexures are discussed in Section 3.

For evaluation of the mechanical design and comparison with the switching current amplifier, a benchmarking linear current amplifier is developed by using a linear PA (OPA544, TI, Texas, USA). This element is attached to a heat sink (SK129, Fischer Elektronik, Luedenscheid, Germany) with a thermal resistance of 4.0 K/W. Integrating a current monitor and control, it regulates the coil current up to 22 kHz (see Fig. 6). To measure the mover's vertical motion z_m with nanometer resolution, a fiber-optic displacement sensor (ATW-01, Unipulse, Tokyo, Japan) with a measurement range of 20 μm is installed. The displacement sensor has high bandwidth of 100 kHz.

3. Mechanical design and analysis

3.1 Model-based analysis For the mechanical design and analysis, the setup is modeled by a lumped mass model in Fig. 2(b) for a small displacement of the mover z_m and the resonator z_r. When the resonator's base is fixed to the mechanical ground (Fig. 2(a)), the resonator's resonant fre-
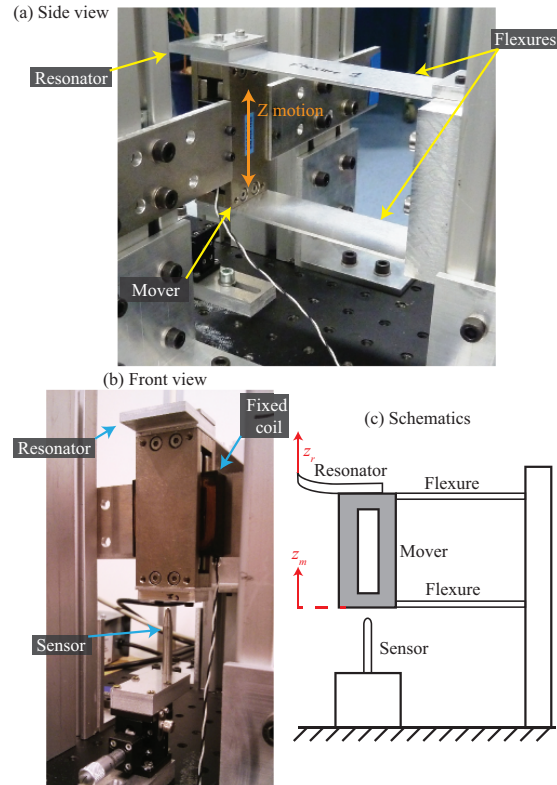

Fig. 1. Experimental setup: (a) side view, (b) front view, and (c) schematics.

quency ω_r is given from the equation of motion by

$$\omega_r = \sqrt{k_r/m_r}, \tag{1}$$

where m_r and k_r are the mass and the stiffness of the resonator, respectively.

When the resonator is mounted onto the mover, as shown in Fig. 2(b), the transfer function $P(s)$ from the actuator force F to the mover position z_m is

$$P(s) = \frac{z_m(s)}{F(s)} = \frac{m_r s^2 + k_r}{m_r m_m s^4 + m_r(k_r + k_f)s^2 + m_m k_r s^2 + k_r k_f}, \tag{2}$$

where the mover mass m_m takes a value of about 0.5 kg, and k_f is the flexure stiffness. The transfer function $P(s)$ has a zero that creates antiresonance at ω_r, which can be used to suppress mechanical vibrations [14]. In this paper, the force ripple induced by the switching PA is filtered.

To filter the force ripple, ω_r in Eq. (1) needs to be relatively high. Thus, assume that k_r is sufficiently higher than k_f. In this case, a resonant frequency at high frequencies ($s = j\omega \gg 0$) given from the denominator of Eq. (2) can be approximated by

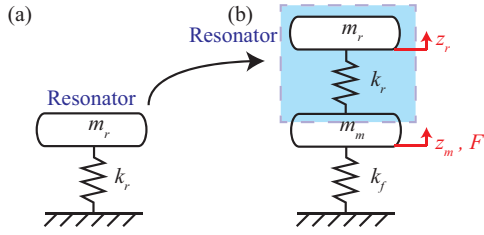$$\omega_2 \approx \sqrt{\frac{k_r(m_r + m_m)}{m_r m_m}}, \tag{3}$$

Integrating PWM amplifier with the design of mechatronic systems for energy-efficient precision motion (Shingo Ito *et al.*)

Fig. 2. Lumped mass model of (a) the resonator and (b) the experimental setup integrating the resonator.

Fig. 3. Resonator: (left) the implemented resonator with the dimensions and (right) the simulated modal shape at the eigenfrequency of 11.7 kHz.

which is due to the decoupling mode of m_r [15]. For high ω_r, m_r needs to be sufficiently lighter than m_m. This implies that the resonance at ω_2 is close to the antiresonance at ω_r in the frequency domain.

Similarly, Eq. (2) is rewritten for the dynamics at relatively low frequencies with $m_m \gg m_r$ as follows:

$$P(s) \approx (m_m s^2 + k_f)^{-1}. \tag{4}$$

The poles of the above equation indicate that the first resonant frequency ω_1 is approximated by $\sqrt{k_f/m_m}$, which is determined by the flexure design. In summary, the above analysis indicates that the antiresonant frequency ω_r to filter the force ripple can be adjusted by the resonator design only. In contrast, the dominant resonant frequency ω_1 is determined mainly by the mover mass and the flexure stiffness. Thus, the resonator and the flexures are independently designed in the following section.

3.2 Mechanical design In high-precision motion control, the high gain of the first mechanical resonance can be utilized to better reject disturbances such as floor vibrations [2]. To utilize the effect, the flexures are designed to set ω_1 between 25 Hz and 40 Hz due to the on-site floor vibrations mainly up to a few tens of Hertz. The design parameters of the leaf-spring flexures are related to ω_1 by Castigliano's second theorem [16] or the bending moment [17] as follows:

$$\omega_1 = \sqrt{\frac{k_f}{m_m}} = \sqrt{\frac{2E w_f h_f^3}{m_m l_f^3}}, \tag{5}$$

where l_f, w_f, and h_f are the length, width, and height of the flexures, respectively. Aluminum sheets are used to implement the flexures, determining Young's modulus $E = 70$ GPa. Eq. (5) is used to roughly tune the dimensions for $\omega_1 = 40$ Hz, and they are fine-tuned by finite element analysis (FEA). The resulting parameters are $l_f = 160$ mm, $w_f = 38.1$ mm, and $h_f = 2.0$ mm.

For simplicity, the resonator is implemented by an aluminum beam, as shown in Fig. 3(left). By using FEA, its length l_r, width w_r, and height h_r are tuned, such that the resulting ω_r takes a sufficiently high value of about 10 kHz. The resulting dimensions are $l_r = 16.5$ mm, $w_r = 38.1$ mm, and $h_r = 5.0$ mm for $\omega_r = 11.7$ kHz. Fig. 3(right) illustrates the simulated corresponding modal shape. The mass of the entire resonator in Fig. 3(left) is about 25 g, which is significantly lighter than m_m, as assumed in Section 3.1.
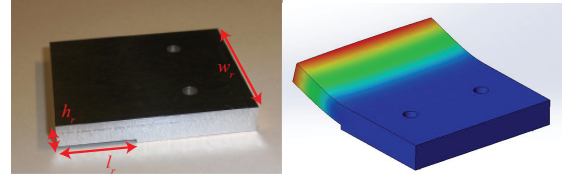
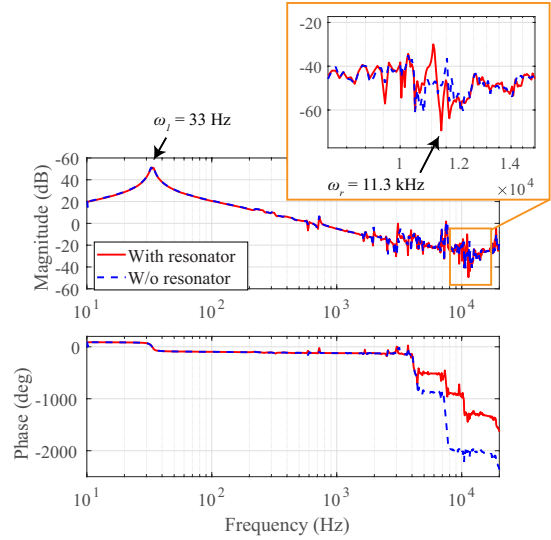**3.3 Validation** To validate the mechanical design,

Fig. 4. Measured frequency response, where the input and the output are the reference to the linear current amplifier and the mover velocity $\dot{z}_m$, respectively.

a frequency response is measured by a system analyzer (3563A, Agilent Technology, Santa Clara, USA). The displacement sensor has a measurement range of only $20\,\mu$m, which is a concern when the mover drifts during measurement. Thus, a laser Doppler vibrometer (OFV-5000, Polytec, Waldbronn, Germany) is used for the frequency response measurement. The resulting Bode plot from the linear current amplifier's reference r_I to the mover velocity $\dot{z}_m$ is shown in Fig. 4, which is measured when the resonator is attached and detached.

As indicated in Fig. 4, the first resonance is visible at 33 Hz, whether the resonator is attached or detached due to its light weight. The measured value is close to the simulated value of 40 Hz, validating the flexure design. The mismatch between the experiment and the simulation may be due to manufacturing and assembly tolerances.

The measured response around 11 kHz is magnified in Fig. 4. It indicates that a notch is created at 11.3 kHz by attaching the resonator to the mover, as desired. Peaks are also visible near the notch. They include the resonance at ω_2 in Eq.(3) and parasitic resonances, such as internal modes of the flexures [17]. To utilize the notch at 11.3 kHz for high precision

Integrating PWM amplifier with the design of mechatronic systems for energy-efficient precision motion (Shingo Ito *et al.*)

(a) Overall system

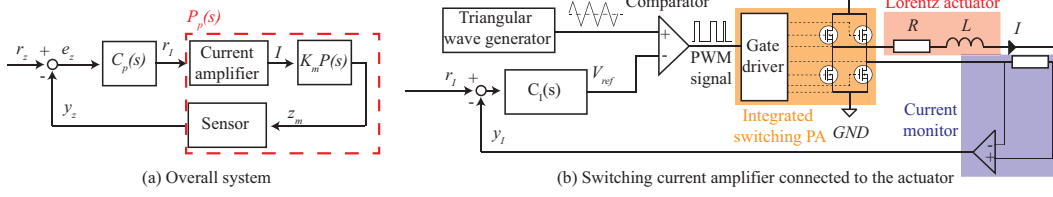(b) Switching current amplifier connected to the actuator

Fig. 5. Block diagram of the system: (a) overall system overview and (b) current amplifier integrating the switching PA.

motion, the switching PA is designed to set the current ripple at that frequency in the next section.

4. Current amplifier design and analysis

Fig. 5(a) shows a block diagram of the entire positioning system. Because its force is proportional to the coil current I, the Lorentz actuator is empowered by a current amplifier. For energy efficiency, a switching PA is utilized in the current amplifier, as shown in Fig. 5(b).

4.1 Switching amplifier As shown in Fig. 5(b), a full bridge inverter circuit is selected for the bidirectional current of the Lorentz actuator. The circuit is implemented by using an IC (L6203, STMicroelectronics, Geneva, Switzerland) including four power transistors and gate drivers. Preventing the IC from overheating, a heat sink with a thermal resistance of 5.6 K/W (6396BG, Aavid, Laconia, USA) is attached. The maximum and minimum voltages applied to the Lorentz coil are determined by the bus voltage V_{DD}, which is set to 15 V.

To filter the force ripple induced by the switching PA, the matching of its switching frequency f_{sw} and ω_r is indispensable. Because setting ω_r accurately is difficult due to the manufacturing and assembly tolerance, f_{sw} must be well-tunable without drift. To satisfy these requirements, PWM [18] is used. To generate the PWM signal for the gate drivers, a triangular wave of f_{sw} is created and compared with the reference V_{ref} by a comparator (Fig. 5(b)). For the accurate tunability of f_{sw} around 10 kHz, the triangular wave generator is implemented by an analog circuit with an integrator, a comparator, and potentiometers.

By applying the small ripple approximation [18], the amplitude of current ripple is given by

$$\Delta_I = \frac{V_{DD} - V_R}{Lf_{sw}}D, \qquad (6)$$

where D and V_R are the duty cycle and the voltage over the resistance R. On an assumption that the coil resistance R is sufficiently small in Eq. (6), the upper bound of the current ripple roughly approximates to 0.9 A_{pp}.

4.2 Current control Since the force of the Lorentz actuator is proportional to the coil current, the coil current I is controlled in the switching current amplifier. For this purpose, I is monitored with a shunt resistor and regulated by a current controller $C_I(s)$. The plant dynamics are dominated by the resistance and inductance of the Lorentz coil and approximated by a first order low-pass filter (LPF). Due to the simple dynamics, a PI controller [19] is implemented by an analog circuit as $C_I(s)$. The PI gains are tuned for the -3 dB bandwidth of 1.7 kHz, as the measured complementary
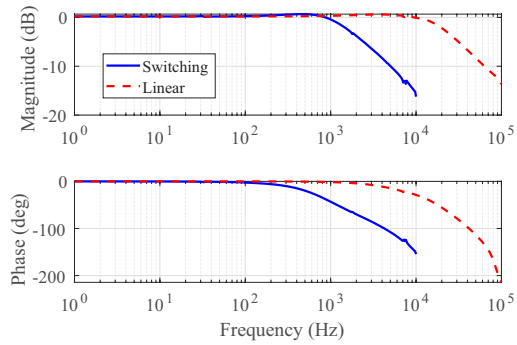

Fig. 6. Measured frequency response of the switching current amplifier from r_I to y_I for current control validation, in comparison with that of the linear amplifier.

sensitivity function is shown in Fig. 6, where the maximum sweep frequency is limited due to f_{sw}.

The current control bandwidth of 1.7 kHz is determined in a tradeoff between the achievable linearity and the achievable motion control bandwidth. Because the switching significantly deforms the coil current at frequencies near f_{sw}, a low current control bandwidth is desired for linearity. In return, a low current control bandwidth results in a phase lag at a relatively low frequency in a frequency response. In the case of Fig. 6, a phase lag is visible at 200 Hz and higher. It restricts the bandwidth of position feedback control to ensure phase margin for closed-loop stability (see Sec. 5).

4.3 Validation Although the triangular wave generator is implemented by the analog circuit for the accurate tunability, a concern of analog circuits in general is thermal drift. Particularly it is problematic when the switching excites the resonances near ω_r in Fig. 4. Therefore, the triangular wave is evaluated by a frequency counter (53220A, Agilent Technology, Santa Clara, USA) to measure f_{sw}. The result reveals that f_{sw} increases by 30 Hz when the triangular wave generator is turned on (cold start). After half an hour, however, f_{sw} is almost constant with fluctuation of less than 1 Hz. For the stable switching frequency, experiments are carried out with hot start.

Since the major concern of the switching current amplifier is the current ripple, it is evaluated. When r_I is set to output a current of -0.5 A at DC, the coil current I is measured as shown in Fig. 7. While the linear current amplifier outputs a smooth current, current ripples are visible with the switching
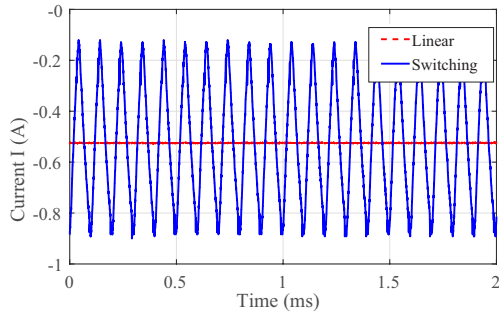
Integrating PWM amplifier with the design of mechatronic systems for energy-efficient precision motion (Shingo Ito *et al.*)

Fig. 7. Measured coil current of the linear and switching amplifier when the reference r_I is set to -0.5 A.
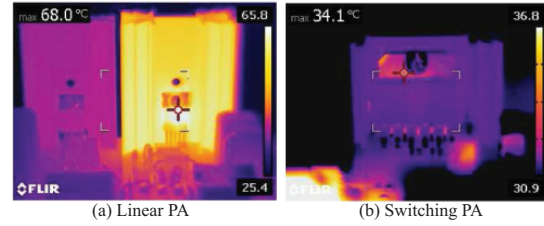

(a) Linear PA   (b) Switching PA

Fig. 8. PAs' temperature measured by a thermal camera when the coil current is 0.4 A at DC: (left) linear PA (OPA544) and (right) switching PA (L6203).

amplifier. Their peak-to-peak amplitude is 0.77 A$_{pp}$.

Another concern of the switching current amplifier is the deformation of the coil current I due to the switching. Thus, total harmonic distortion (THD) of I is measured by the system analyzer when the reference I_r is set to output a sinusoidal current with an amplitude of 0.2 A at 10 Hz, 100 Hz, and 1 kHz. Table 1 lists the measured THD using the first 20th harmonics in comparison with the linear current amplifier. While the switching current amplifier's THD is as low as the linear current amplifier at 10 Hz and 100 Hz, it is degraded to 4 % at 1 kHz. To prevent further deformation of the current at higher frequencies, the 1.7 kHz bandwidth is useful, as desired in the current control design.

Table 1. Measured THD comparing the switching and linear current amplifiers.

Frequency of 0.2 A sinusoidal current	10 Hz	100 Hz	1 kHz
Linear current amp.	0.2 %	0.2 %	0.3 %
Switching current amp.	0.2 %	0.4 %	4.0 %

Finally, to investigate the effectiveness of the switching on the energy dissipation, the temperature of the linear and switching PAs is measured by a thermal camera (E60bx, FLIR, Wilsonville, USA) when the current amplifiers output 0.4 A at DC at a room temperature of $T_r = 23\,°C$. For a fair comparison with the switching PA with $V_{dd} = 15V$, the power supply of the linear PA is set to ± 15 V. As seen in Fig. 8(a), the linear PA has a relatively high temperature of 68 °C, heating up the entire heat sink. In contrast, the switching PA has a significantly lower temperature of 34.1°C only, although its heat sink has a higher thermal resistance.

By applying a lumped model, the power Q dissipated by a PA through its heat sink is approximated by [20]

$$Q \approx (T_h - T_r)/R_{th}, \tag{7}$$

where T_h and R_{th} are the temperature and the thermal resistance of the heat sink, respectively. By using Eq. (7), the dissipated power by the linear PA is estimated at 11.3 W. This large wasted power is significantly decreased by a factor of 5.6 to 2.0 W by using the switching PA, demonstrating its high energy efficiency.

5. Motion control

High precision motion systems typically have different types of disturbances such as thermal drift and floor vibrations. They have to be compensated to evaluate the influence of the current ripple on the mover position. In order to do so, a position feedback controller $C_p(s)$ is used, as shown in Fig. 5(a). To achieve a closed-loop bandwidth above ω_1 without a steady state error, a tamed PID controller [15] [21] is selected as $C_p(s)$ and given by

$$C_p(s) = K_p + \frac{K_i}{s} + \frac{K_d s}{K_a s + 1}, \tag{8}$$

where the PID gains are denoted by K_p, K_i, and K_d, and the parameter K_a determines the frequency to terminate the derivative action.

To determine the controller parameters, the plant model $P_p(s)$ is derived by curve fitting with a measured Bode plot from r_I to the displacement sensor's output y_z (see Fig. 5), as shown in Fig. 9. Based on a simulated open-loop transfer function $L_p(s) = C_p(s)P_p(s)$, the controller parameters are tuned to maximize the open-loop crossover frequency with a sufficient phase margin. The tuned parameters are $K_p = 0.429$, $K_i = 41.4$, $K_d = 7.94 \times 10^{-4}$, and $K_a = 2.39 \times 10^{-4}$. The corresponding $C_p(s)$ and $L_p(s)$ are simulated in Fig. 9, which indicates the open-loop crossover frequency at 200 Hz with a phase margin of 36 degrees.

The designed controller $C_p(s)$ is implemented by an analog circuit (cf. [15]), which is advantageous for high-precision positioning, without generating quantization noise unlike digital filters. For validation, the complementary sensitivity function from the position reference r_z to the mover position z_m is measured, and it follows the trend of the simulation, as shown in Fig. 10. The experimental result indicates that the achieved -3 dB closed-loop bandwidth is 290 Hz. Additionally, Fig. 11 shows the measured and simulated sensitivity function, which quantifies the disturbance rejection performance. It is visible that $C_p(s)$ rejects disturbances such as floor vibrations up to about 100 Hz. Notice that the wide notch around 30 Hz is realized for good disturbance rejection by the control design with the resonance at ω_1, as intended in the flexure design.

6. Experiments

While the switching PA decreases the dissipated energy by a factor of 5.6, its switching results in the current ripple of 0.77 A$_{pp}$. In order to investigate its influence on the positioning resolution, the mover position z_m is measured by the displacement sensor while the position feedback control is active. This measurement is carried out for two cases: when
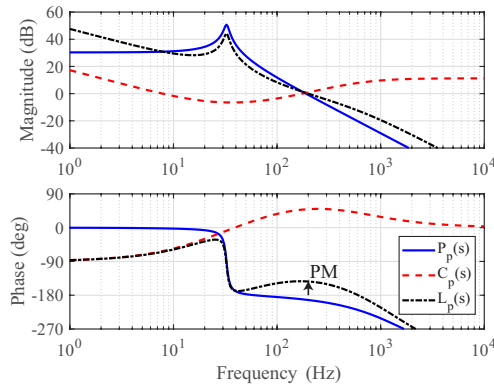
Fig. 9. Simulated Bode plots of the plant model $P_p(s)$, the designed position feedback controller $C_p(s)$, and the open-loop transfer function $L_p(s)$. The arrow indicates a phase margin (PM) of 36 degrees.
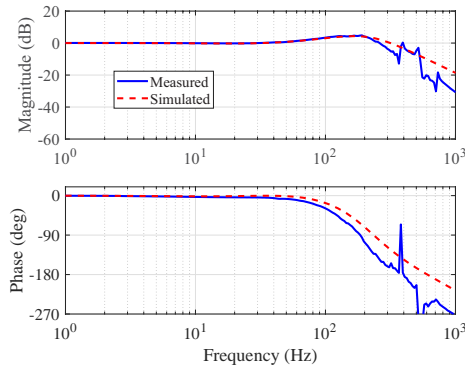

Fig. 10. Measured and simulated complementary sensitivity function from the position reference r_z to the mover position z_m.
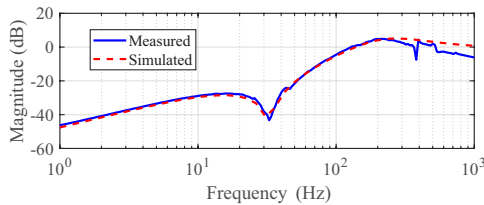

Fig. 11. Measured and simulated sensitivity function of the position loop, which corresponds a frequency response from the position reference r_z to the position error e_z.

the antiresonance is utilized to filter the force ripple by setting f_{sw} to the mechanical notch frequency $\omega_r = 11.3$ kHz and when the antiresonance is not used by setting f_{sw} to 10.3 kHz.

As shown in Fig. 12, the power spectral density (PSD) of the displacement sensor's output y_z is measured by the system analyzer. It is clearly visible that the usage of the antiresonance successfully decreases the harmonic around 10 kHz approximately from -80 dB to -110 dB. It can also be seen
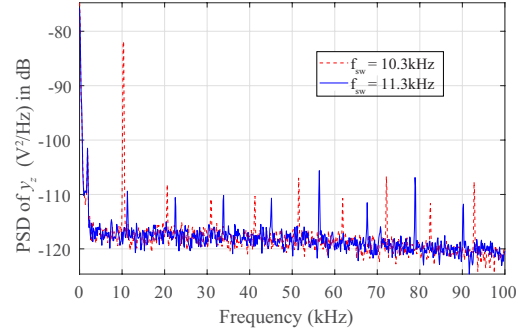

Fig. 12. Measured PSD of the displacement sensor output when f_{sw} is set to 11.3 kHz for the antiresonance and 10.3 kHz for comparison.

that the noise floor gradually decreases as the frequency increases, which would be due to the displacement sensor's bandwidth (100 kHz). Nevertheless, the harmonic peaks increase at high frequencies; hence, they are assumed as the switching noise due to EMI.

Fig. 13 shows the measured z_m in the time domain where pulses of approximately ±80 nm would be the noise due to EMI. To evaluate the mover position without the EMI noise, the measured z_m is filtered offline by a zero-phase third-order LPF [22] with a cutoff frequency of 100 kHz, which corresponds to the displacement sensor's bandwidth. The filtered signals are shown in Fig 14. In the case of $f_{sw} = 10.3$ kHz, the switching results in a position ripple of approximately 10 nm, and the calculated root mean square (RMS) is 5.1 nm. This position ripple is eliminated by setting f_{sw} to 11.3 kHz. Consequently, the RMS is successfully decreased by 69 % to 1.6 nm.

The effectiveness is further confirmed by step responses in Fig. 15. When f_{sw} is set to 10.3 kHz in Fig. 15(top), the measured position has a band of about 15 nm$_{pp}$. It is visible in Fig. 15(bottom) that the band gets narrower by setting f_{sw} to 11.3 kHz for the utilization of the antiresonance. Note that Fig. 15 additionally shows a motion error at relatively low frequencies. It would be due to the disturbances such as residual floor vibrations, and they can be rejected, for example by using feedforward control with a vibration sensor [2]. Overall, the experimental results demonstrate that energy-efficient high-precision positioning is realized by the proposed mechatronic system design integrating the switching current amplifier and the mechanical notch filter.

7. Conclusion

Simultaneously improving the energy efficiency and the current resolution of a PA is challenging to drive a Lorentz actuator for high-precision motion control. In fact, in comparison with the comparable linear current amplifier, the designed switching current amplifier is able to decrease the power dissipation by a factor of 5.6, however, resulting in the current ripple of 0.77 A$_{pp}$.

To realize high precision motion in an energy efficient way despite the current ripple, this paper proposes an integrated mechatronic system design that filters the force rip-
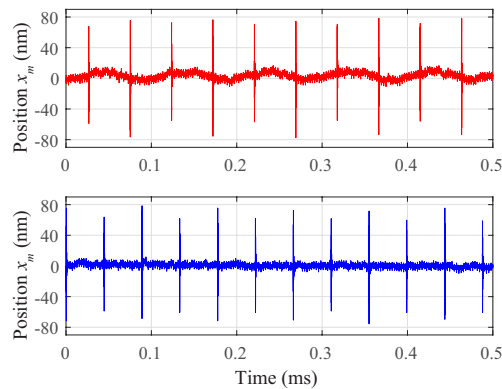
Fig. 13. Measured mover position: (top) without using the antiresonance by setting f_{sw} to 10.3 kHz and (bottom) with the utilized antiresonance setting f_{sw} to 11.3 kHz.
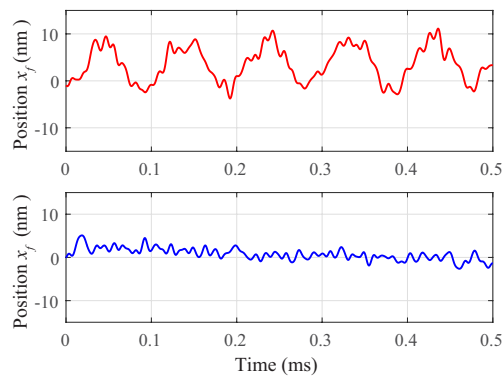

Fig. 14. Measured mover position that is filtered by a 100 kHz LPF to eliminate EMI noise: (top) without using the antiresonance by setting f_{sw} to 10.3 kHz and (bottom) with the utilized antiresonance by setting f_{sw} to 11.3 kHz.
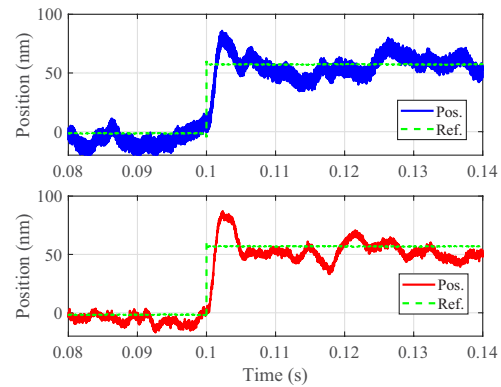

Fig. 15. Measured step response that is filtered by a 100 kHz LPF to eliminate EMI noise: (top) without using the antiresonance by setting f_{sw} to 10.3 kHz and (bottom) with the utilized antiresonance by setting f_{sw} to 11.3 kHz.

ple induced by the switching current amplifier. For the experimental demonstration, a positioning system is developed with a flexure-guided Lorentz actuator, which is controlled by a position feedback controller. To realize the force filter, a resonator is mounted onto the mover, creating an antiresonance at 11.3 kHz. By setting the switching frequency of the switching current amplifier, the oscillation of the mover due to the current ripple is successfully suppressed. Consequently, the positioning error is improved from 5.1 nm to 1.6 nm.

Acknowledgment

References

(1) T. Ando, "High-speed atomic force microscopy and its future prospects," *Biophysical Reviews*, vol. 10, pp. 285–292, Apr 2018.

(2) S. Ito and G. Schitter, "Atomic force microscopy capable of vibration isolation with low-stiffness z-axis actuation," *Ultramicroscopy*, vol. 186, pp. 9–17, 2018.

(3) J. Stampfl, R. Liska, and A. Ovsianikov, *Multiphoton Lithography: Techniques, Materials and Applications.* Wiley-VCH, 2016.

(4) S. Ito and G. Schitter, "Comparison and classification of high-precision actuators based on stiffness influencing vibration isolation," *IEEE/ASME Transactions on Mechatronics*, vol. 21, no. 2, pp. 1169–1178, 2016.

(5) A. Okyay, K. Erkorkmaz, and M. B. Khamesee, "Mechatronic design, actuator optimization, and control of a long stroke linear nano-positioner," *Precision Engineering*, vol. 52, pp. 308 – 322, 2018.

(6) S. Ito, S. Troppmair, B. Lindner, F. Cigarini, and G. Schitter, "Long-range fast nanopositioner using nonlinearities of hybrid reluctance actuator for energy efficiency," *IEEE Transactions on Industrial Electronics*, vol. 66, no. 4, pp. 3051–3059, 2019.

(7) S. Hadian and K. Madani, "A system of systems approach to energy sustainability assessment: Are all renewables really green?," *Ecological Indicators*, vol. 52, pp. 194 – 206, 2015.

(8) E. McCune, "A technical foundation for RF CMOS power amplifiers: Part 2: Power amplifier architectures," *IEEE Solid-State Circuits Magazine*, vol. 7, pp. 75–82, Fall 2015.

(9) E. McCune, "Power amplifier efficiency ceilings due to signal modulation type," in *European Microwave Conference*, pp. 1132–1135, Oct 2017.

(10) Kok Kiong Tan, Tong Heng Lee, Hui Fang Dou, Shok Jun Chin, and Shao Zhao, "Precision motion control with disturbance observer for pulsewidth-modulated-driven permanent-magnet linear motors," *IEEE Transactions on Magnetics*, vol. 39, pp. 1813–1818, May 2003.

(11) Y. Jiao and F. C. Lee, "LCL filter design and inductor current ripple analysis for a three-level NPC grid interface converter," *IEEE Transactions on Power Electronics*, vol. 30, no. 9, pp. 4659–4668, 2015.

(12) B. Reznikov, M. Srndovic, Y. L. Familiant, G. Grandi, and A. Ruderman, "Simple time averaging current quality evaluation of a single-phase multilevel PWM inverter," *IEEE Transactions on Industrial Electronics*, vol. 63, pp. 3605–3615, June 2016.

(13) D. Han, S. Li, Y. Wu, W. Choi, and B. Sarlioglu, "Comparative analysis on conducted CM EMI emission of motor drives: WBG versus Si devices," *IEEE Transactions on Industrial Electronics*, vol. 64, pp. 8353–8363, Oct 2017.

(14) A. Hassan, A. Torres-Perez, S. Kaczmarczyk, and P. Picton, "Vibration control of a stirling engine with an electromagnetic active tuned mass damper," *Control Engineering Practice*, vol. 51, pp. 108 – 120, 2016.

(15) R. Munnig Schmidt, G. Schitter, A. Rankers, and J. van Eijk, *The Design of High Performance Mechatronics.* Delft University Press, 2nd revised edition ed., 2014.

(16) B. J. Kenton and K. K. Leang, "Design and control of a three-axis serial-kinematic high-bandwidth nanopositioner," *IEEE/ASME Transactions on*

Integrating PWM amplifier with the design of mechatronic systems for energy-efficient precision motion (Shingo Ito *et al.*)

Mechatronics, vol. 17, no. 2, pp. 356–369, 2012.
(17) S. Ito, F. Cigarini, S. Unger, and G. Schitter, "Flexure design for precision positioning using low-stiffness actuators," *IFAC-PapersOnLine*, vol. 49, no. 21, pp. 200 – 205, 2016. 7th IFAC Symposium on Mechatronic Systems MECHATRONICS 2016.
(18) R. W. Erickson and D. Maksimovic, *Fundamentals of Power Electronics*. Springer, 2001.
(19) A. Matsubara, *Design and Control of Precision Positioning and Feed Drive Systems (in Japanese)*. Morikita Publishing Co., Ltd., 2008.
(20) J. Choi, M. Jeong, J. Yoo, and M. Seo, "A new CPU cooler design based on an active cooling heatsink combined with heat pipes," *Applied Thermal Engineering*, vol. 44, pp. 50 – 56, 2012.
(21) S. Ito, S. Unger, and G. Schitter, "Vibration isolator carrying atomic force microscope's head," *Mechatronics*, vol. 44, pp. 32–41, 2017.
(22) F. Gustafsson, "Determining the initial states in forward-backward filtering," *IEEE Transactions on Signal Processing*, vol. 44, pp. 988–992, April 1996.

Shingo Ito (Non-member) received the MASc in Mechanical and Industrial Engineering from the University of Toronto, Canada, in 2007 and the PhD in Electrical Engineering from TU Wien, Vienna, Austria in 2015. From 2007 to 2010, he served as an engineer in the field of motion control at Yaskawa Electric Corporation, Iruma, Saitama, Japan.
He is currently a postdoctoral researcher at the Automation and Control Institute (ACIN), TU Wien. His research interest includes design and control of high-precision mechatronic systems for production, inspection, and automation, such as atomic force microscopes, laser scanners, and 3D printers.

Stefan Pirker (Non-member) received the MSc in Automation Technology in 2015 from TU Wien, Vienna Austria. His research for the Master's degree focused on the design and control of high-precision actuators at the Automation and Control Institute (ACIN), TU Wien.
Currently he serves as a systems engineer at in-tech engineering GmbH, Vienna Austria. Performing safety engineering and safety management during the development of rail and automotive vehicles such as trains, metros, cars and buses.

Georg Schitter (Non-member) Georg Schitter is Professor for Advanced Mechatronic Systems at the Automation and Control Institute (ACIN) of TU Wien. He received an MSc in Electrical Engineering from TU Graz, Austria (2000) and an MSc and PhD degree from ETH Zurich, Switzerland (2004).
His primary research interests are on high-performance mechatronic systems, particularly for applications in the high-tech industry, scientific instrumentation, and mechatronic imaging systems, such as AFM, scanning laser and LIDAR systems, telescope systems, adaptive optics, and lithography systems for semiconductor industry. He received the journal best paper award of IEEE/ASME Transactions on Mechatronics (2017), of the IFAC Mechatronics (2008-2010), of the Asian Journal of Control (2004-2005), and the 2013 IFAC Mechatronics Young Researcher Award. He served as an Associate Editor for IFAC Mechatronics, Control Engineering Practice, and for the IEEE Transactions on Mechatronics.